

Electrical Control over Phonon Polarization in Strained Graphene

J. Sonntag,^{1,2,*} S. Reichardt,³ B. Beschoten,¹ and C. Stampfer^{1,2}

¹*JARA-FIT and 2nd Institute of Physics, RWTH Aachen University, 52074 Aachen, Germany*

²*Peter Grünberg Institute (PGI-9), Forschungszentrum Jülich, 52425 Jülich, Germany*

³*Department of Physics and Materials Science, University of Luxembourg, L-1511 Luxembourg, Luxembourg*
(Dated: March 12, 2022)

We explore the tunability of the phonon polarization in suspended uniaxially strained graphene by magneto-phonon resonances. The uniaxial strain lifts the degeneracy of the LO and TO phonons, yielding two cross-linearly polarized phonon modes and a splitting of the Raman G peak. We utilize the strong electron-phonon coupling in graphene and the off-resonant coupling to a magneto-phonon resonance to induce a gate-tunable circular phonon dichroism. This, together with the strain-induced splitting of the G peak, allows us to controllably tune the two linearly polarized G mode phonons into circular phonon modes. We are able to achieve a circular phonon polarization of up to 36 % purely by electrostatic fields and can reverse its sign by tuning from electron to hole doping. This provides unprecedented electrostatic control over the angular momentum of phonons, which paves the way towards phononic applications.

Phonons – collective excitations of lattice vibrations – play a fundamental role in solid state physics and materials science. They affect a wide variety of material properties and phenomena relevant for electronics, thermal transport as well as optics [1, 2], and are pivotal for quantum effects such as superconductivity. Of particular interest are material systems in which phonons carry additional degrees of freedom, such as chirality [3–5], polarization, or angular momentum [6, 7]. They are crucial for novel phonon-driven phenomena such as the phonon Hall effect [8, 9], the phonon ac Stark [10] and Edelstein effects [11], or the phonon Zeeman effect [12] and can even drive electronic phase transitions [13, 14] and topological states [15]. A control over phonons and their degrees of freedom is thus a key goal on the pathway to potential phononic applications [1, 2], such as phonon-based quantum information devices [16]. However, a microscopic control over phonons is very challenging due to their spin-less nature and the large inertia of the nuclei, which makes phonons effectively charge-less and thus hard to control directly with electromagnetic fields. In systems with strong electron-phonon interaction, however, a control over phonons can be achieved by tuning the electronic system. In this regard, graphene is a prime candidate as it features strong electron-phonon interaction due to its two-dimensional nature and allows for excellent external control over its electronic system. In particular, the degenerate longitudinal (LO) and transverse optical (TO) phonons at the Γ point of the first Brillouin zone are strongly coupled to the electronic system, which enables the tuning of their frequencies and lifetimes via an electrostatic gate [17]. The electron-phonon coupling can further be significantly enhanced or quenched by a large external magnetic field, where the electronic system condenses into discrete Landau levels, giving rise to so-called magneto-phonon resonances (MPRs) [18–31].

Here, we show that we can tune the polarization of the optical phonons from linear to circular via a com-

bination of static electric and magnetic fields, yielding control over the phonon angular momentum. The initial linear phonon polarization results from an uniaxial strain ($\approx 0.8\%$), which lifts the degeneracy of the LO and TO phonons and polarizes the modes parallel and perpendicular to the orientation of the strain [32, 33]. We circularly polarize the phonons by exploiting their coupling to selected Landau level transitions, which we control via an electrostatic gate [29–31]. To monitor the degeneracy-lifted phonon modes, we employ confocal Raman spectroscopy and track the phonon polarization by means of a few-level system model.

To start with, we consider the LO/TO phonons at the Γ point, which give rise to the so-called G peak in the Raman spectrum of graphene. In pristine, unstrained graphene, these phonons are degenerate and the doublet exhibits continuous rotation symmetry. As such, the two modes may be described by any linearly independent combination of in-plane vectors $\mathbf{v}_{G\pm}$. Two common choices are the Cartesian basis $\hat{\mathbf{x}}, \hat{\mathbf{y}}$, depicted in Figures 1a,b and the circular basis $\sigma^\pm = (\hat{\mathbf{x}} \pm i\hat{\mathbf{y}})/\sqrt{2}$. The latter basis represents a circular motion of the atoms in (counter-)clockwise directions (Figures 1e,f), which results in an angular momentum of the two modes of $\pm 1\hbar$. We subject the graphene to uniaxial strain to linearly polarize the phonon modes parallel and perpendicular to the strain direction [32, 33], as illustrated in Figures 1c,d. This also lifts the degeneracy of the G mode phonons and splits the G peak into two separate peaks denoted by G^\pm with frequencies ω_{G+} and ω_{G-} , which enables us to differentiate the response of the two phonon modes and track changes in their polarization. To gain control over the polarization of the phonons we exploit their coupling to the electronic system, which can be readily manipulated via a static electromagnetic fields. In particular, we use an out-of-plane magnetic field B to quantize the electronic density of states into Landau levels (LLs) and control their occupancies via tuning the charge carrier

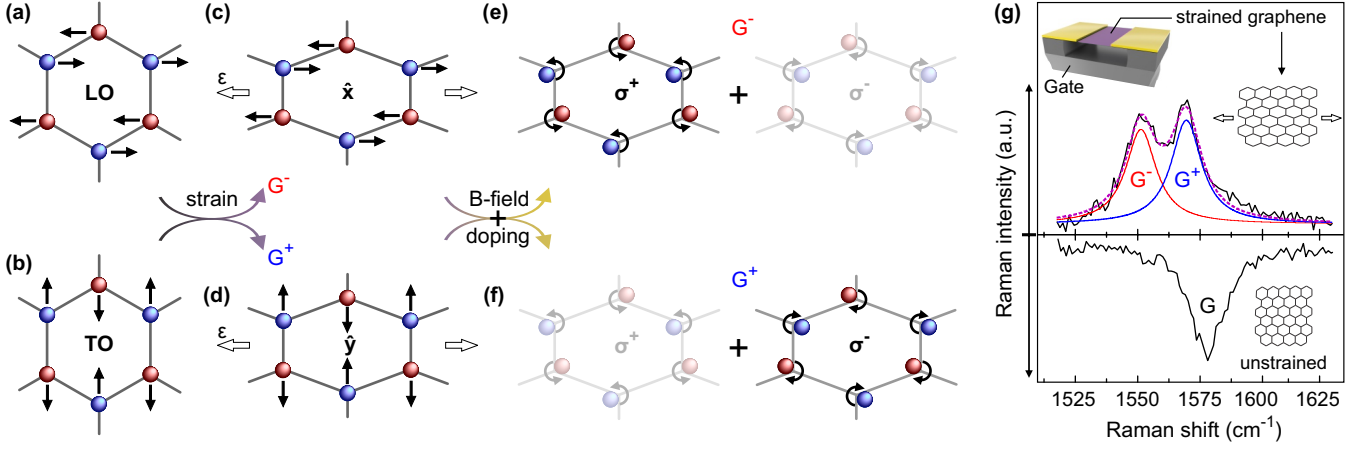


FIG. 1. (a-d) Illustration of the degenerate LO and TO phonon modes that give rise to the G peak in the linear basis \hat{x}, \hat{y} before (a,b) and after (c,d) the application of uniaxial strain ϵ . (e,f) Illustration of the induced circular polarization of the phonon modes when tuning the electronic system with a magnetic field B and with a electrostatically induced charge carrier density n (doping). The level of opaqueness indicates the weight of the respective circular polarization in the modes. (g) Raman spectrum of graphene featuring the G peak before (bottom) and after (top) the current annealing step. The purple line represents a fit to the two subpeak-structure with a sum of two Lorentzians (red and blue dotted lines). Upper left inset: Schematic illustration of graphene (purple) suspended from two gold contacts (yellow). The current annealing step induces uniaxial strain illustrated by the two right insets.

density n with a gate voltage. This way, we can selectively Pauli-block circularly polarized LL transitions and, via their coupling to the phonons, induce a net circular phonon polarization into the split modes, as schematically depicted in Figures 1e,f.

Our experiments are based on a suspended graphene field effect device, see schematic in the inset of Figure 1g. It features a high charge carrier mobility and a low charge carrier density inhomogeneity, both of which are crucial to observe magneto-phonon resonances. A current-annealing step is employed to both induce uniaxial strain and to effectively clean the graphene sheet [34], leading to a sharp peak in device resistance at the charge neutrality point and a charge carrier inhomogeneity of $n^* \approx 5.5 \times 10^9 \text{ cm}^{-2}$ (see Figure S1 in Supporting Information). The presence of uniaxial strain after annealing is clearly visible in the splitting of the Raman G peak into two separate peaks, see Figure 1g. To quantify the peak splitting and the induced strain, we fit the G peak with a sum of two Lorentzians which share the same spectral width Γ_G . The two subpeaks are centered around a mean frequency of $\bar{\omega}_G \approx 1566.4 \text{ cm}^{-1}$ and split by $\Delta\omega_G \approx 14.8 \text{ cm}^{-1}$. From $\Delta\omega_G$ we estimate the amount of uniaxial strain in our sample as $\epsilon \approx 0.82 \%$ [35], where we used the previously measured Grüneisen parameters $\partial\omega_{G^+}/\partial\epsilon \approx -18.6 \text{ cm}^{-1}/\%$ and $\partial\omega_{G^-}/\partial\epsilon \approx -36.4 \text{ cm}^{-1}/\%$ [32]. This significant amount of uniaxial strain induced by the current annealing step is in line with a recent report by Jung *et al.* [36].

We now turn to the control over the linearly polarized G mode phonons via the manipulation of the electronic system. To this end, we first focus on magneto-

phonon resonances, i.e. the coupling of the phonons to the circularly polarized LL transitions, by measuring the B field dependence of the linearly polarized modes at the charge neutrality point ($E_F = 0$). Here, no phonon dichroism and thus no circular phonon polarization is expected due to the electron-hole symmetry. The measured Raman spectra for magnetic fields ranging from 0 to 7.5 T (and taken at $\approx 4.2 \text{ K}$) are depicted in Figure 2a. Both the strain-induced splitting of the G peak into the G^+ and G^- peaks and the resonant coupling to LL transitions at $B \approx 3 \text{ T}$ are clearly visible. The magneto-phonon resonance at $B \approx 3 \text{ T}$ is the so-called T_1 resonance [18, 24, 25, 27]. It occurs when the phonon energy $E_G = \hbar\omega_G(B=0, n=0)$ matches the energy difference between two LLs with energies $E_j = \pm v_F \sqrt{2e\hbar B} \cdot j$, where v_F is the Fermi velocity and j is the LL index. The most prominent T_j -MPRs involve LL transitions $-j \rightarrow j+1$ (T_j^+) and $-j-1 \rightarrow j$ (T_j^-) with an orbital angular momentum of $\pm \hbar$ [24, 25]. These transitions couple to the respective circularly polarized phonons σ^\pm , see Figure 2b. The corresponding energies and the resonance condition are then given by

$$T_j = E_{j+1} - E_{-j} = v_{T_j} \sqrt{2e\hbar B} (\sqrt{j+1} + \sqrt{j}) = E_G. \quad (1)$$

The lower panel in Figure 2c visualizes this resonance condition. Note that we replaced v_F by the effective Fermi velocity v_{T_j} , which can generally be a function of n , B , and the LL index j , due to many-body and excitonic effects [27, 37, 38]. To highlight the coupling of the two phonon modes to the LL transitions, we extract their frequency shifts $\Delta\omega_{G^\pm} = \omega_{G^\pm} - \omega_0^\pm$ relative to their respective frequencies at $B = 0 \text{ T}$ as well as their

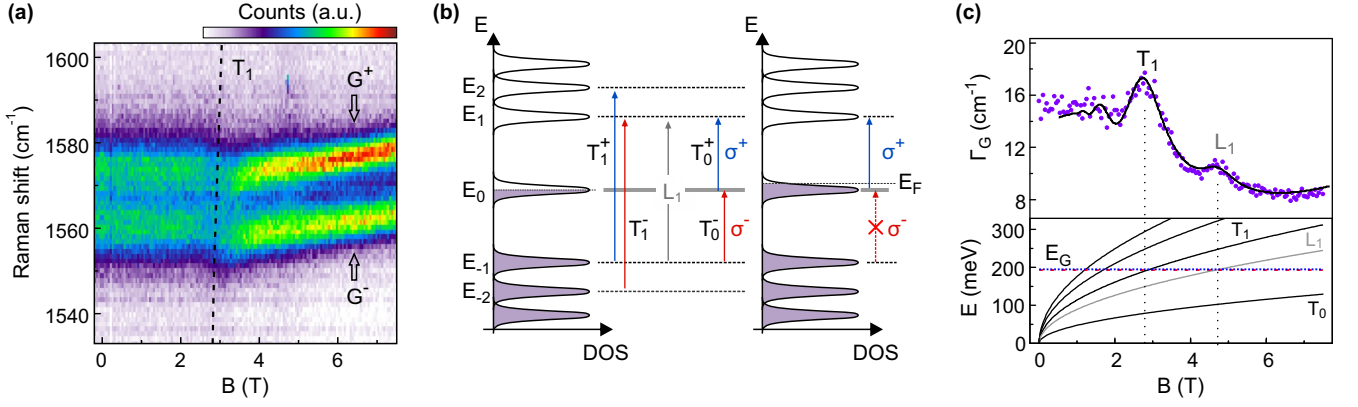


FIG. 2. (a) Raman intensity around the strain-split G peak of graphene as a function of B -field at $n \approx 0$ (highlighting the G^- and G^+ peak). (b) Illustration of the electronic transitions of the dominating MPRs and the density of states. Transitions with $\Delta j = (-)1$ only couple to right (left) circularly polarized phonons $\sigma^{+(-)}$, color coded as blue (red). (c) Lower panel: Interband LL transition energies T_n (solid lines) and L_1 (grey, dotted lines). The closely spaced dashed red and dotted blue lines indicate the energies of the G^- and G^+ mode phonons at $B = 0$ T, respectively. The energy of the most relevant T_1 resonance is also shown in (a) as a dashed line. Upper panel: B -field dependent width Γ_G of the two subpeaks G^- and G^+ . The black line represents a fit based on Dyson's equation.

shared width $\Gamma_G = \Gamma_{G^+} = \Gamma_{G^-}$ by fitting the sum of two Lorentzians. Most noticeably, the coupling leads to a decrease of the phonon lifetime at the resonance due to the excitation of electron-hole pairs, which results in the increased width Γ_G of both modes at the T_1 resonance, see upper panel in Figure 2c. We also observe a minor contribution of the L_1 ($-1 \rightarrow 1$) transition at $B \approx 4.7$ T, which is usually forbidden due to the conservation of angular momentum, but can occur due to higher order processes [24]. The magnetic field $B_{T_1} = 2.73$ T at which the T_1 -MPRs occurs corresponds to an effective Fermi velocity of $v_{T_1} \approx 1.35 \times 10^6$ m/s, see Equation 1. Although strain has been predicted to change v_F [39, 40], we find that this value of v_F is in excellent agreement to previous results on the Fermi velocity renormalization in the presence of LLs in unstrained graphene [27].

As shown in Figure 3a we observe identical magneto-phonon resonances of the two cross-linearly polarized G^- and G^+ phonon modes at $n = 0$. Note that the splitting of $\Delta\omega_G = 14.8$ cm⁻¹ is larger than the axis range in Figures 3a-c. This indicates that the strain-induced splitting dominates over the individual phonon frequency renormalization from the MPR. This can be intuitively understood because at zero doping, the electron-hole symmetry is not broken and the T_1^\pm LL transitions remain degenerate and couple with equal strength to the phonons [31]. As a result, there is no circular phonon dichroism and thus no circular phonon polarization at $n = 0$. In this regime we can describe the MPRs by calculating the phonon self-energy and solving Dyson's equation [18, 24, 25] (see Supporting Information for a more detailed discussion). A combined fit of the solution of the Dyson's equation to both ω_{G^-} and Γ_G is shown as black lines in Figure 2d and Figure 3a. Evidently, the fit

describes the ω_{G^+} just as well.

In the following, we show that a net circular phonon polarization can be induced by electrostatic gating, i.e. by tuning the system to a finite charge carrier density n . After briefly discussing the influence of n on T_1 , we will particularly focus on the gate-tunable off-resonant coupling of the phonons to the T_0^\pm transition, which occurs at large B -fields, $B \approx 20$ T. Here, the finite n breaks the symmetry of T_0^\pm , which results in a circular phonon dichroism and thereby a circular phonon polarization.

Figures 3b,c show that the T_1 -MPR gradually vanishes for higher charge carrier densities for both G^- and G^+ . This is a consequence of the Pauli blocking of the respective transition (see Figure 2b). An electron density of $n \approx 0.7 \times 10^{12}$ cm⁻² corresponds to a filling factor $\nu = nh/(eB) \approx 10$ at $B \approx 3$ T, which leaves the second LL completely filled and blocks both the $-2 \rightarrow 1$ and the $-1 \rightarrow 2$ transitions in Figure 3c. Notably, we observe a significant increase in $\Delta\omega_G$ at higher magnetic fields even at high $|n|$, which we attribute to the tail of the T_0 resonance at $B \approx 20$ T. Note, that the T_0 resonance becomes unblocked as the effective filling factor decreases with B , see also black dotted lines in Figure 3d-f. Most strikingly, we observe that the evolution of the two phonon modes $\Delta\omega_{G^-}$ and $\Delta\omega_{G^+}$ split for large magnetic fields. This is most pronounced at an intermediate electron density of $n \approx 0.3 \times 10^{12}$ cm⁻² (see Figure 3b). The splitting can be attributed to the charge-carrier dependent change of the coupling strengths of the T_0^\pm transitions resulting in a net circular phonon polarization. For increasing n , the coupling to the T_0^+ transition increases due to the increasing number of states partaking (see Fermi level shift for electron doping in Figure 2b). This leads to an enhanced anti-crossing for the σ^+ phonon branch, which

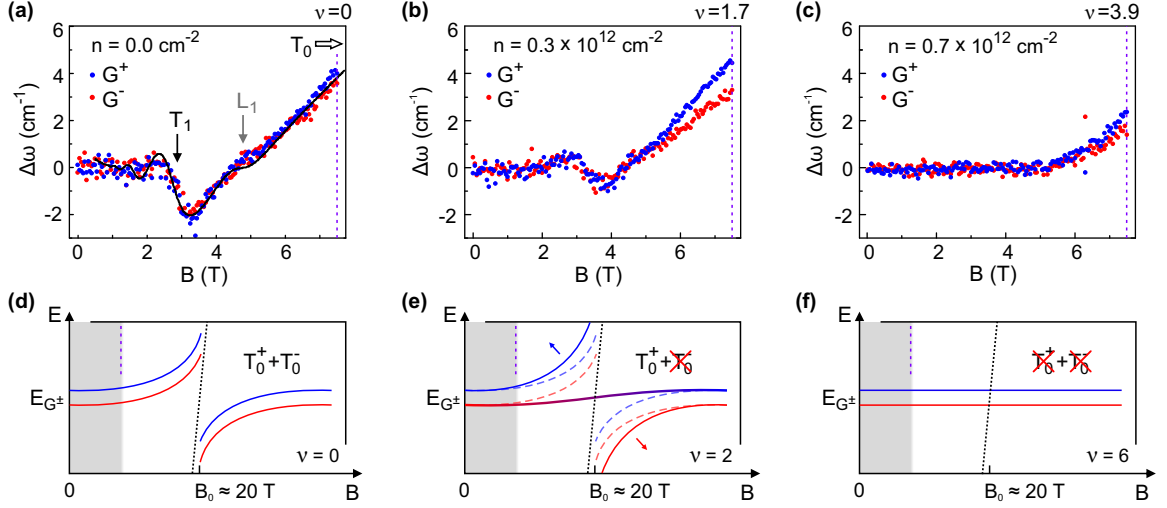


FIG. 3. (a) Change in phonon frequency $\Delta\omega$ as a function of B field for both the G^- (red) and the G^+ mode (blue) at $n \approx 0$. The absolute shift between the two modes is 14.8 cm^{-1} . The black line represents a fit based on Dysons's equation. (b) and (c) show the same measurement as (a), but at intermediate and high n , respectively. (d-f) Illustration of the effect of the filling factor on the T_0 -MPR. The colored lines are $E_G^\pm = \hbar\omega_G^\pm$ and the dashed black line is T_0 . At $\nu = 2$ (e) the T_0^- transition is completely blocked while the T_0^+ increases in strength. For comparison the $\nu = 0$ case shown in (d) is reproduced in (e) as colored dotted lines. (f) At $\nu = 6$ all relevant LLs are completely filled and no transitions are possible. Note that ν is assumed to be constant for all B for clarity. The area shaded in grey illustrates the measurement range shown in panels (a-c).

is illustrated for a constant filling factor of $\nu = 2$ in Figure 3d-f. Compared to the situation for filling factor $\nu = 0$, the enhanced anti-crossing leads to an increase in ω_{G^+} for frequencies below the resonance (blue curve), up to a density where the second LL is completely filled and the coupling strength decreases again, resulting in a reduction of ω_{G^+} for $\nu > 2$. In contrast, the T_0^- transition is suppressed by filling the zeroth LL (Figure 2b), resulting in a weaker anti-crossing for σ^- (see Figure 3e), i.e., a monotonic decrease in ω_{G^-} . Indeed, as seen in Figure 4a, both the G^- and G^+ phonons show a qualitatively different dependence on n at $B = 7.5 \text{ T}$, which is a result of the doping-induced phonon dichroism. While ω_{G^-} monotonically decreases in frequency with increasing $|n|$, ω_{G^+} first increases for small $|n|$ before declining at larger densities. As indicated by the grey lines in Figure 4a, the maxima in ω_{G^+} are located precisely at the complete filling of the zeroth LL at $n \approx 0.3 \times 10^{12} \text{ cm}^{-2}$.

In the following, we introduce and discuss an effective six-stage model to quantitatively describe the qualitatively different behaviour of ω_{G^\pm} . Importantly, we show that the G^+ -peak obtains a large electric field-tunable circular phonon polarization. Within the model, the coupled electron-phonon system is described by six coupled quantum mechanical states. They represent the two phonon modes, the two T_0 -, and the two T_1 -LL excitations, which couple to each other with coupling strengths $g_{T_j^\pm}$. We choose to represent the phonon modes in their circular basis σ^\pm to easily include the selection rules resulting from the conservation of angular momentum, i.e., the σ^+ phonon only couples to the T_j^+ ($-j \rightarrow j+1$) tran-

sition. In the basis $(\sigma^+, \sigma^-, T_0^+, T_0^-, T_1^+, T_1^-)$ the Hamiltonian is given by:

$$H = \begin{pmatrix} \hbar\omega_0 & \hbar\eta & g_{T_0^+} & 0 & g_{T_1^+} & 0 \\ \hbar\eta & \hbar\omega_0 & 0 & g_{T_0^-} & 0 & g_{T_1^-} \\ g_{T_0^+} & 0 & \hbar\omega_{T_0} & 0 & 0 & 0 \\ 0 & g_{T_0^-} & 0 & \hbar\omega_{T_0} & 0 & 0 \\ g_{T_1^+} & 0 & 0 & 0 & \hbar\omega_{T_1} & 0 \\ 0 & g_{T_1^-} & 0 & 0 & 0 & \hbar\omega_{T_1} \end{pmatrix} - i\frac{\hbar}{2}\Gamma, \quad (2)$$

where $\Gamma = \text{diag}(\gamma_{\text{ph}}, \gamma_{\text{ph}}, \gamma_{T_0}, \gamma_{T_0}, \gamma_{T_1}, \gamma_{T_1})$ is a diagonal matrix that describes the broadening of the phonons and electronic transitions. $\omega_0 = E_G/\hbar$ and $\omega_{T_j} = T_j/\hbar$ are the bare phonon and LL transition frequencies, respectively. η is a parameter which describes the strain-induced splitting of the two modes. The coupling constants between the phonons and LL transitions depend on the electron-phonon coupling constant λ , the magnetic field B , and the filling of the LLs [18, 24, 25]:

$$g_{T_j^\pm} = \sqrt{\bar{\nu}_{T_j^\pm} \lambda / 2 T_0} = \nu_F \sqrt{\bar{\nu}_{T_j^\pm} \lambda e \hbar B}. \quad (3)$$

See also the discussion in the Supporting Information. Here, the effective partial filling factor of the LL transitions $\bar{\nu}_{T_j^\pm}$ are a function of the magnetic field and are given by:

$$\begin{aligned} \bar{\nu}_{T_j^+} &= (1 + \delta_{j,0})(\bar{\nu}_{-j} - \bar{\nu}_{j+1}), \\ \bar{\nu}_{T_j^-} &= (1 + \delta_{j,0})(\bar{\nu}_{-(j+1)} - \bar{\nu}_{+j}). \end{aligned} \quad (4)$$

The partial filling factor $\bar{\nu}_j$ relates the filling factor ν to the fractional occupancy of the j th LL:

$$\bar{\nu}_j = \frac{\nu + 2 - 4j}{4} \Big|_{\in[0,1]}, \quad (5)$$

which is defined as $\bar{\nu}_j = 0$ if $\nu + 2 - 4j/4 < 0$ and $\bar{\nu}_j = 1$ if $\nu + 2 - 4j/4 > 1$ and considers the spin and valley degeneracy of graphene. We are now able to calculate the energies of the phonon modes under the influence of the coupling to the T_0^\pm and T_1^\pm transitions by numerically diagonalizing Equation 2. To this end, we use the experimental parameters extracted from the fit shown in Figure 2d and Figure 3a at $n = 0$, which results in effective Fermi velocities [41] $v_{T_1} \approx 1.35 \times 10^6$ m/s and $v_{L_1} \approx 1.23 \times 10^6$ m/s, an electronic broadening of the T_j -transitions $\gamma_{T_j} \approx 392$ cm $^{-1}$ and L_1 -transition $\gamma_{L_1} \approx 196$ cm $^{-1}$, a phonon broadening $\gamma_{ph} \approx 2.5$ cm $^{-1}$, an electron-phonon coupling constant $\lambda = 4.5 \times 10^{-3}$ [17, 42], and a coupling strength of the L_1 -transition $\lambda_L \approx 0.27 \times 10^{-3}$. Further, we assume $v_{T_0} = v_{L_1}$, $\gamma_{T_0} = \gamma_{L_1}$ and use $\eta = 8.6$ cm $^{-1}$.

Evidently, we find good agreement between our model and our experimental data, as shown in Figure 4a. Crucially, we observe the initial increase in ω_{G^+} with $|n|$ and the kinks of ω_{G^\pm} at $|\nu| = 2$. As discussed previously, the coupling of the circular $\sigma^{+(-)}$ phonon to the $T_0^{+(-)}$ -transition increases (decreases) with electron doping $n > 0$ as more (less) electronic states become available (compare the sketch in Figure 2b and the corresponding effective LL transition filling factors $\bar{\nu}_{T_j}$ in Figure 4b and their connection to the coupling constants $g_{T_j^\pm}$ in Equation 3). At $n = 0$ the G^+ peak has equal weights of σ^\pm , which cancels these effects. However, at larger electron doping $n > 0$, the σ^+ -phonon shows an increased frequency due to a stronger anti-crossing with the T_0^+ -transition, caused by an increased coupling strength, as illustrated in Figure 3e. This results in an increase of the σ^+ -polarization of the G^+ -mode. To calculate the net circular phonon polarization, we first obtain the weight of the σ^\pm component in the G^\pm mode by projection on the respective component: $w(\sigma^\pm, G^\pm) = |\sigma^\pm \cdot \mathbf{v}_{G^\pm}|^2$. We then define the circular polarization of the G^\pm modes as

$$P_{G^\pm} = \frac{w(\sigma^+, G^\pm) - w(\sigma^-, G^\pm)}{w(\sigma^+, G^\pm) + w(\sigma^-, G^\pm)} = 2w(\sigma^+, G^\pm) - 1. \quad (6)$$

Here, we made use of the fact that both weights need to add up to one: $w(\sigma^+, G^\pm) + w(\sigma^-, G^\pm) = 1$. Note that in the interacting electron-phonon system, this identity does no longer hold exactly, as the phonon states can now contain an admixture of electronic excitations, but it is still a very good approximation in the off-resonant electron-phonon coupling regime considered here. For the phonon weights, we find values above 0.65 as shown in Figure 4c, corresponding to a maximum circular polarization $P_{G^+} \approx 36\%$ of the G^+ -mode at $\nu = 2$. For $\nu > 2$

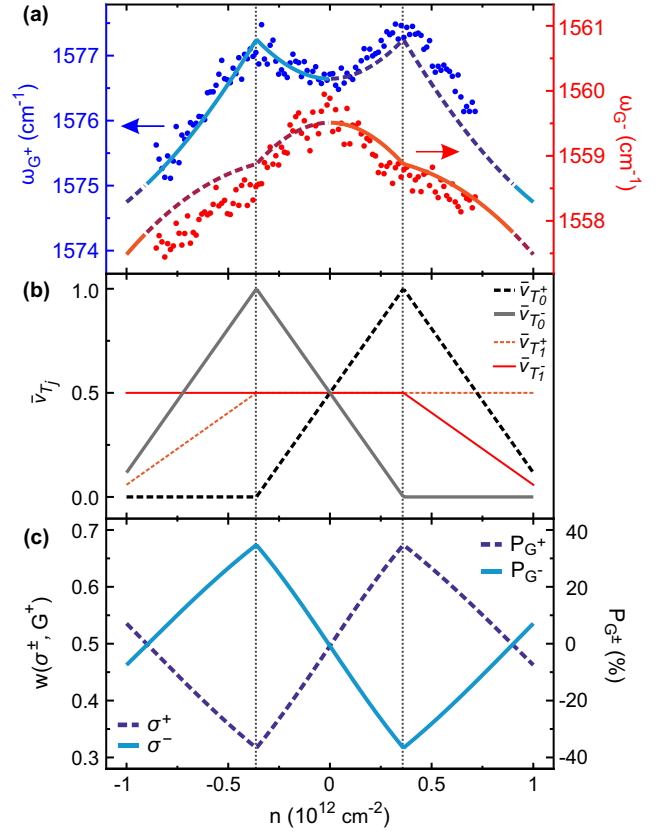


FIG. 4. (a) Measured frequencies of the G^+ (blue dots, left axis) and the G^- modes (red dots, right axis) as a function of charge carrier density n . The grey dashed lines mark a filling factor $|\nu| = 2$, i.e., a complete filling of the zeroth LL. The lines show ω_{G^\pm} as calculated via Equation 2. The dotted (dark solid) lines correspond to the phonon mode where σ^+ (σ^-) predominates. (b) Effective partial filling factor of the LL transitions $\bar{\nu}_{T_j^\pm}$ as a function of n at $B = 7.5$ T. (c) Weights of σ^\pm in the G^+ -mode. The G^- -mode shows the exact opposite behavior. The right axis shows the corresponding polarization P_{G^\pm} of the two subpeaks G^\pm .

the effective filling factor $\bar{\nu}_{T_0^+}$ (see Figure 4b) decreases and with it the coupling strength $g_{T_0^+}$. This results in a weakening of the anti-crossing and thus in a decreased ω_{G^+} and decreased phonon polarization. Since the G^- -mode will always be predominantly polarized as a circular phonon with lower coupling strength for each B -field below the resonant magnetic field, it shows a monotonic decrease as function of ω_{G^-} . It is important to emphasize that the $T_0^{+(-)}$ -transitions swap their roles when going from electron ($n > 0$) to hole doping ($n < 0$), i.e., for hole doping, the G^+ mode will be σ^- -polarized. This results in the same polarization behavior, albeit with opposite sign. Consequently, we are uniquely able to tune the circular polarization of the G^\pm -modes, reaching polarization degrees of up to 36 %, purely by static electro-magnetic fields due to the interplay of the strain-induced

splitting of the phonon modes and the doping-induced circular dichroism of the phonons. We are thus able to control the angular momentum of the phonons, which is directly related to the polarization $P_{G\pm}$.

In conclusion, we explored the coupling of strain-split linearly polarized phonons to circularly polarized Landau level transitions in graphene. We showed that even off-resonant effects can play a crucial role in the understanding of the electron-phonon coupling in graphene, as the high B -field T_0 -MPR has a significant impact on the phonon modes even at moderate magnetic fields of $B = 7.5$ T. We have shown that by electrostatic doping, we can selectively couple the phonons to specific Landau level transitions, inducing a net circular phonon polarization. The breaking of the electron-hole symmetry in combination with the application of uniaxial strain allows us to control the phonon polarization from a purely linear to a circular polarization of up to 36 %, purely by electrostatic fields. We expect that this control of the phonon polarization and angular momentum by static electromagnetic fields will be of great interest for phononic applications [4, 5]. Moreover, our observation of MPRs in strained graphene shows that MPRs can be a viable tool in the future to investigate strain gradient-induced pseudo-magnetic fields [43].

METHODS

Sample fabrication: The suspended graphene sample is fabricated from an exfoliated graphene flake on Si/SiO₂. The contacts made from Cr/Au are fabricated via electron beam-lithography and a subsequent lift-off step. The flake is suspended by etching away ~ 170 nm of SiO₂ with hydrofluoric acid. A final critical point drying-step is used to prevent the collapse of the suspended graphene flakes. The graphene flake investigated here has a width of $2\ \mu\text{m}$ and the distance between the contacts is $1.5\ \mu\text{m}$.

Raman measurements: The magneto-Raman measurements are performed in a confocal, low-temperature ($T = 4.2$ K) micro-Raman setup, which is equipped with a superconducting magnet as well as electrical feedthroughs to conduct combined optical and transport experiments. The laser ($\lambda = 532$ nm) has a power of 0.5 mW and is focused to a spot size of ~ 500 nm. All Raman spectra are taken in the center of the graphene flake.

Acknowledgments: The authors thank S. Staacks for help on the figures. This project has received funding from the European Union's Horizon 2020 research and innovation programme under grant agreement No 881603 (Graphene Flagship), the Deutsche Forschungsgemeinschaft (DFG, German Research Foundation; STA 1146/12-1) and support by the Helmholtz Nanoelectronic Facility (HNF) [44] at the Forschungszentrum Jülich.

-
- * Corresponding author: sonntag@physik.rwth-aachen.de
- [1] M. Maldovan, "Sound and heat revolutions in phononics," *Nature* **503**, 209–217 (2013).
 - [2] N. Li, J. Ren, L. Wang, G. Zhang, P. Hänggi, and B. Li, "Colloquium: Phononics: Manipulating heat flow with electronic analogs and beyond," *Rev. Mod. Phys.* **84**, 1045–1066 (2012).
 - [3] H. Chen, W. Zhang, Q. Niu, and L. Zhang, "Chiral phonons in two-dimensional materials," *2D Mater.* **6**, 012002 (2018).
 - [4] H. Zhu, J. Yi, M.-Y. Li, J. Xiao, L. Zhang, C.-W. Yang, R. A. Kaindl, L.-J. Li, Y. Wang, and X. Zhang, "Observation of chiral phonons," *Science* **359**, 579–582 (2018).
 - [5] D. Liu and J. Shi, "Circular phonon dichroism in Weyl semimetals," *Phys. Rev. Lett.* **119**, 075301 (2017).
 - [6] D. M. Juraschek and N. A. Spaldin, "Orbital magnetic moments of phonons," *Phys. Rev. Mater.* **3**, 064405 (2019).
 - [7] B. Cheng, T. Schumann, Y. Wang, X. Zhang, D. Barbalas, S. Stemmer, and N. P. Armitage, "A Large Effective Phonon Magnetic Moment in a Dirac Semimetal," *Nano Lett.* **20**, 5991–5996 (2020).
 - [8] L. Zhang, J. Ren, J.-S. Wang, and B. Li, "Topological Nature of the Phonon Hall Effect," *Phys. Rev. Lett.* **105**, 225901 (2010).
 - [9] C. Strohm, G. L. J. A. Rikken, and P. Wyder, "Phenomenological Evidence for the Phonon Hall Effect," *Phys. Rev. Lett.* **95**, 155901 (2005).
 - [10] V. L. Korenev, M. Salewski, I. A. Akimov, V. F. Sapega, L. Langer, I. V. Kalitukha, J. Debus, R. I. Dzhiyev, D. R. Yakovlev, D. Müller, C. Schröder, H. Hövel, G. Karczewski, M. Wiater, T. Wojtowicz, Yu. G. Kusrayev, and M. Bayer, "Long-range p-d exchange interaction in a ferromagnet-semiconductor hybrid structure," *Nat. Phys.* **12**, 85–91 (2016).
 - [11] M. Hamada, E. Minamitani, M. Hirayama, and S. Murakami, "Phonon Angular Momentum Induced by the Temperature Gradient," *Phys. Rev. Lett.* **121**, 175301 (2018).
 - [12] D. M. Juraschek, M. Fechner, A. V. Balatsky, and N. A. Spaldin, "Dynamical multiferroicity," *Phys. Rev. Mater.* **1**, 014401 (2017).
 - [13] M. Först, R. Mankowsky, and A. Cavalleri, "Mode-Selective Control of the Crystal Lattice," *Acc. Chem. Res.* **48**, 380–387 (2015).
 - [14] M. Rini, R. Tobey, N. Dean, J. Itatani, Y. Tomioka, Y. Tokura, R. W. Schoenlein, and A. Cavalleri, "Control of the electronic phase of a manganite by mode-selective vibrational excitation," *Nature* **449**, 72–74 (2007).
 - [15] G. Jotzu, M. Messer, R. Desbuquois, M. Lebrat, T. Uehlinger, D. Greif, and T. Esslinger, "Experimental realization of the topological Haldane model with ultracold fermions," *Nature* **515**, 237–240 (2014).
 - [16] K. C. Lee, M. R. Sprague, B. J. Sussman, J. Nunn, N. K. Langford, X.-M. Jin, T. Champion, P. Michelberger, K. F. Reim, D. England, D. Jaksch, and I. A. Walmsley, "Entangling Macroscopic Diamonds at Room Temperature," *Science* **334**, 1253–1256 (2011).
 - [17] S. Pisana, M. Lazzeri, C. Casiraghi, K. S. Novoselov, A. K. Geim, A. C. Ferrari, and F. Mauri, "Breakdown of the adiabatic Born-Oppenheimer approximation in

- graphene,” *Nat. Mater.* **6**, 198–201 (2007).
- [18] C. Neumann, S. Reichardt, M. Drögeler, B. Terrés, K. Watanabe, T. Taniguchi, B. Beschoten, S. V. Rotkin, and C. Stampfer, “Low B Field Magneto-Phonon Resonances in Single-Layer and Bilayer Graphene,” *Nano Lett.* **15**, 1547–1552 (2015).
- [19] J. Yan, S. Goler, T. D. Rhone, M. Han, R. He, P. Kim, V. Pellegrini, and A. Pinczuk, “Observation of Magnetophonon Resonance of Dirac Fermions in Graphite,” *Phys. Rev. Lett.* **105**, 227401 (2010).
- [20] Y. Kim, J. M. Poumirol, A. Lombardo, N. G. Kalugin, T. Georgiou, Y. J. Kim, K. S. Novoselov, A. C. Ferrari, J. Kono, O. Kashuba, V. I. Fal’ko, and D. Smirnov, “Measurement of Filling-Factor-Dependent Magnetophonon Resonances in Graphene Using Raman Spectroscopy,” *Phys. Rev. Lett.* **110**, 227402 (2013).
- [21] C. Faugeras, M. Amado, P. Kossacki, M. Orlita, M. Kühne, A. A. L. Nicolet, Yu. I. Latyshev, and M. Potemski, “Magneto-Raman Scattering of Graphene on Graphite: Electronic and Phonon Excitations,” *Phys. Rev. Lett.* **107**, 036807 (2011).
- [22] S. Goler, J. Yan, V. Pellegrini, and A. Pinczuk, “Raman spectroscopy of magneto-phonon resonances in graphene and graphite,” *Solid State Commun.* **152**, 1289–1293 (2012).
- [23] C. Faugeras, M. Amado, P. Kossacki, M. Orlita, M. Sprinkle, C. Berger, W. A. de Heer, and M. Potemski, “Tuning the Electron-Phonon Coupling in Multilayer Graphene with Magnetic Fields,” *Phys. Rev. Lett.* **103**, 186803 (2009).
- [24] T. Ando, “Magnetic Oscillation of Optical Phonon in Graphene,” *J. Phys. Soc. Jpn.* **76**, 024712 (2007).
- [25] M. O. Goerbig, J.-N. Fuchs, K. Kechedzhi, and Vladimir I. Fal’ko, “Filling-factor-dependent magnetophonon resonance in graphene,” *Phys. Rev. Lett.* **99**, 087402 (2007).
- [26] C. Faugeras, M. Orlita, and M. Potemski, “Raman scattering of graphene-based systems in high magnetic fields,” *J. Raman Spectrosc.* **49**, 146–156 (2018).
- [27] J. Sonntag, S. Reichardt, L. Wirtz, B. Beschoten, M. I. Katsnelson, F. Libisch, and C. Stampfer, “Impact of Many-Body Effects on Landau Levels in Graphene,” *Phys. Rev. Lett.* **120**, 187701 (2018).
- [28] C. Faugeras, P. Kossacki, A. A. L. Nicolet, M. Orlita, M. Potemski, A. Mahmood, and D. M. Basko, “Probing the band structure of quadri-layer graphene with magneto-phonon resonance,” *New J. Phys.* **14**, 095007 (2012).
- [29] P. Kossacki, C. Faugeras, M. Kühne, M. Orlita, A. Mahmood, E. Dujardin, R. R. Nair, A. K. Geim, and M. Potemski, “Circular dichroism of magnetophonon resonance in doped graphene,” *Phys. Rev. B* **86**, 205431 (2012).
- [30] P. Leszczynski, Z. Han, A. A. L. Nicolet, B. A. Piot, P. Kossacki, M. Orlita, V. Bouchiat, D. M. Basko, M. Potemski, and C. Faugeras, “Electrical Switch to the Resonant Magneto-Phonon Effect in Graphene,” *Nano Lett.* **14**, 1460–1466 (2014).
- [31] O. Kashuba and V. I. Fal’ko, “Interplay between uniaxial strain and magnetophonon resonance in graphene,” *Phys. Rev. B* **87**, 161404 (2013).
- [32] T. M. G. Mohiuddin, A. Lombardo, R. R. Nair, A. Bonetti, G. Savini, R. Jalil, N. Bonini, D. M. Basko, C. Galiotis, N. Marzari, K. S. Novoselov, A. K. Geim, and A. C. Ferrari, “Uniaxial strain in graphene by Raman spectroscopy: *G* peak splitting, G_{r} uneisen parameters, and sample orientation,” *Phys. Rev. B* **79**, 205433 (2009).
- [33] N. S. Mueller, S. Heeg, M. P. Alvarez, P. Kusch, S. Wasserroth, N. Clark, F. Schedin, J. Parthenios, K. Papagelis, C. Galiotis, M. Kalbáč, A. Vijayaraghavan, U. Huebner, R. Gorbachev, O. Frank, and S. Reich, “Evaluating arbitrary strain configurations and doping in graphene with Raman spectroscopy,” *2D Mater.* **5**, 015016 (2017).
- [34] K. I. Bolotin, K. J. Sikes, Z. Jiang, M. Klima, G. Fudenberg, J. Hone, P. Kim, and H. L. Stormer, “Ultrahigh electron mobility in suspended graphene,” *Solid State Commun.* **146**, 351–355 (2008).
- [35] Note that we discard the possibility of additional biaxial strain here, which is unlikely to be present in our sample due to the device geometry. Furthermore, biaxial strain would result in a constant shift of both subpeaks, which is irrelevant for the main experimental findings and the polarisation analysis performed here.
- [36] M. Jung, P. Rickhaus, S. Zihlmann, A. Eichler, P. Makk, and C. Schönenberger, “GHz nanomechanical resonator in an ultraclean suspended graphene p–n junction,” *Nanoscale* **11**, 4355–4361 (2019).
- [37] C. Faugeras, S. Berciaud, P. Leszczynski, Y. Henni, K. Nogajewski, M. Orlita, T. Taniguchi, K. Watanabe, C. Forsythe, P. Kim, R. Jalil, A. K. Geim, D. M. Basko, and M. Potemski, “Landau Level Spectroscopy of Electron-Electron Interactions in Graphene,” *Phys. Rev. Lett.* **114**, 126804 (2015).
- [38] L. A. Chizhova, J. Burgdörfer, and F. Libisch, “Magneto-optical response of graphene: Probing substrate interactions,” *Phys. Rev. B* **92**, 125411 (2015).
- [39] S.-M. Choi, S.-H. Jhi, and Y.-W. Son, “Effects of strain on electronic properties of graphene,” *Phys. Rev. B* **81**, 081407 (2010).
- [40] F. de Juan, M. Sturla, and M. A. H. Vozmediano, “Space Dependent Fermi Velocity in Strained Graphene,” *Phys. Rev. Lett.* **108**, 227205 (2012).
- [41] For a more stable fit we assumed the same $v_{T_j} = v_{T_1}$ for all j expect for $j = 0$, which shares $v_{T_0} = v_{L_1}$, since T_0 shares the first LL with L_0 .
- [42] Guillaume Froehlicher and Stéphane Berciaud, “Raman spectroscopy of electrochemically gated graphene transistors: Geometrical capacitance, electron-phonon, electron-electron, and electron-defect scattering,” *Phys. Rev. B* **91**, 205413 (2015).
- [43] G. J. Verbiest, S. Brinker, and C. Stampfer, “Uniformity of the pseudomagnetic field in strained graphene,” *Phys. Rev. B* **92**, 075417 (2015).
- [44] Wolfgang Albrecht, Juergen Moers, and Bernd Hermanns, “HNF-Helmholtz Nano Facility,” *Journal of large-scale research facilities* **3**, 112 (2017).

Supporting Information: Electrical Control over Phonon Polarization in Strained Graphene

PHONON SELF-ENERGY FOR LINEAR PHONON POLARIZATION

The evolution of the linearly polarized G mode phonon frequency and width with magnetic field and doping can be obtained by solving Dyson's equation

$$(\hbar\omega)^2 - (\hbar\tilde{\omega}_0)^2 - 2\hbar\tilde{\omega}_0\Pi(\omega) = 0 \quad (\text{S1})$$

for the complex phonon frequency $\omega = \omega_G - i\Gamma_G/2$. Here, $\tilde{\omega}_0 = \omega_0 - i\gamma_{\text{ph}}/2$, where ω_0 is the phonon frequency in the absence of a magnetic field and at zero doping in the adiabatic approximation and γ_{ph} accounts for the non-electronic contribution to the phonon decay width. $\Pi(\omega)$ denotes the phonon self-energy for linear phonon polarization and is the same both x - and y -polarization. It can be derived from the microscopic coupling of the Landau levels to the phonon within a tight binding-based model for the electron-phonon interaction [18, 24, 25] and can be written as

$$\Pi(\omega) = \lambda \frac{T_0^2}{4} \sum_{s=\pm} \sum_{j=0}^{\infty} \left[\bar{\nu}_{T_j^s} \frac{2\tilde{T}_j}{(\hbar\omega)^2 - \tilde{T}_j^2} + \frac{2}{\tilde{T}_j} \right]. \quad (\text{S2})$$

Here, $\tilde{T}_j = T_j - i\hbar\gamma_{T_j}/2$ is the complex T_j transition energy that includes a finite decay width γ_{T_j} . The partial filling factors $\bar{\nu}_{T_j^s}$ have been defined in the main text, while λ is a dimensionless effective electron-phonon coupling constant. Finally, the experimentally observable, but in a first approximation symmetry-forbidden, L_j ($-j \rightarrow +j$) transitions can be included phenomenologically via the replacement

$$\Pi(\omega) \rightarrow \Pi(\omega) + \lambda_L T_0^2 \sum_{j=0}^{\infty} \left[\bar{\nu}_{L_j} \frac{2\tilde{L}_j}{(\hbar\omega)^2 - \tilde{L}_j^2} + \frac{2}{\tilde{L}_j} \right], \quad (\text{S3})$$

with the respective partial filling factors being given by $\bar{\nu}_{L_j} = (\bar{\nu}_{-j} - \bar{\nu}_{+j})$ and the complex transition energies being given by $\tilde{L}_j = E_{+j} - E_{-j} - i\hbar\gamma_{L_j}/2$.

DETAILS OF THE SIX-LEVEL MODEL

The six-level model is based on the effective Hamiltonian

$$\hat{H} = \sum_{s=\pm} \hbar\omega_0 \hat{b}_s^\dagger \hat{b}_s + \hbar\eta \left(\hat{b}_+^\dagger \hat{b}_- + \hat{b}_-^\dagger \hat{b}_+ \right) + \sum_{\substack{s=\pm \\ j=0,1}} T_j \hat{d}_{T_j^s}^\dagger \hat{d}_{T_j^s} + \sum_{\substack{s=\pm \\ j=0,1}} g_{T_j^s} \left(\hat{b}_s^\dagger \hat{d}_{T_j^s} + \hat{d}_{T_j^s}^\dagger \hat{b}_s \right), \quad (\text{S4})$$

which is written in terms of the creation and annihilation operators for the circularly polarized phonon modes, $\hat{b}_\pm^{(\dagger)}$, and for the $T_{j=0,1}$ LL transitions, $\hat{d}_{T_j^\pm}^{(\dagger)}$. The first term describes the uncoupled circularly polarized phonon modes, while the second term represents the strain-induced coupling between them. The latter can be derived by considering a strain-induced phonon frequency splitting of 2η in a linear basis and then rotating the Hamiltonian in a linear basis into the circular basis. The third term in Equation S4 describes the uncoupled T_j^\pm transitions, whereas the last term accounts for the electron-phonon coupling between phonons and the LL transitions, which is diagonal in the σ^\pm basis.

The effective, doping-dependent coupling constants $g_{T_j^\pm}$ can be derived by rotating the microscopic LL electron-phonon matrix elements for linear phonon polarization into the circular basis. Alternatively, they can simply be read off by noting that the phonon self-energy for linear phonon polarization is the average of the phonon self-energies for circular polarization:

$$\Pi(\omega) = \frac{1}{2} [\Pi_+(\omega) + \Pi_-(\omega)] = \frac{1}{2} \sum_{s=\pm} \sum_{j=0}^{\infty} \left[g_{T_j^s}^2 \frac{2\tilde{T}_j}{(\hbar\omega)^2 - \tilde{T}_j^2} + g_{T_j^s}^2 \Big|_{n=0} \frac{2}{\tilde{T}_j} \right], \quad (\text{S5})$$

from which we can identify $g_{T_j^\pm} = T_0 \sqrt{\bar{\nu}_{T_j^\pm} \lambda / 2}$.

TRANSPORT MEASUREMENTS AND ADDITIONAL RAMAN MEASUREMENTS

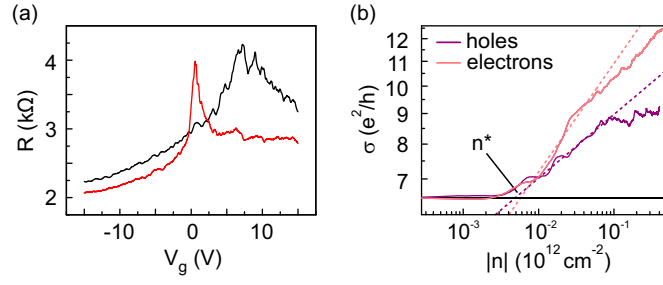


FIG. S1. (a) The resistance as a function of V_g before (black) and after current annealing (red). (b) Double logarithmic plot of σ after current annealing versus charge carrier density $|n|$ for determining the charge carrier inhomogeneity n^* .

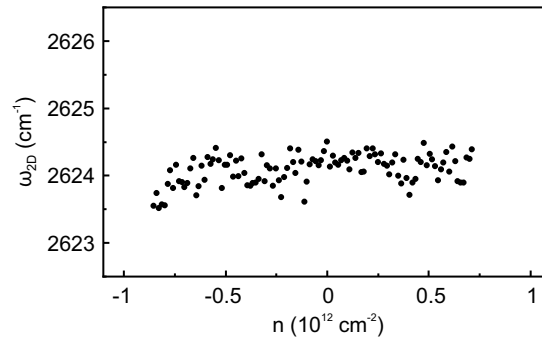


FIG. S2. The 2D-peak position ω_{2D} does not show significant variation as a function of n indicating a negligible amount of gate-induced strain.